A Joint Geochemical-Geophysical Record of Time-Dependent Mantle Convection South of Iceland: Supplementary Material

S. M. Jones[a,b,*], B. J. Murton[c], J. G. Fitton[d], N. J. White[e], J. Maclennan[e], R. L. Walters[f,b]

[a] *University of Birmingham, School of Geography, Earth & Environmental Sciences, Edgbaston, Birmingham B15 2TT, United Kingdom.*
[b] *Previous address: Trinity College Dublin, School of Natural Sciences, Department of Geology, Dublin 2, Ireland.*
[c] *National Oceanography Centre, Southampton, University of Southampton Waterfront Campus, European Way, Southampton SO14 3ZH, United Kingdom.*
[d] *University of Edinburgh, School of GeoSciences, Grant Institute, The King's Buildings, West Mains Road, Edinburgh EH9 3JW, United Kingdom.*
[e] *University of Cambridge, Department of Earth Sciences, Bullard Laboratories, Madingley Road, Cambridge CB3 0EZ, United Kingdom.*
[f] *Department of Geological Sciences, University of Florida, 241 Williamson Hall, Gainesville, Florida 32611-2120, US.*

Abstract

This supplementary material contains the following.
A. Analytical Geochemical Techniques
B. Composition and Melting: Additional Figures
C. Method of Comparing Modelled and Observed Compositions
D. Method of Estimating Plume Volume Flux

Keywords: Mantle convection, mid-ocean ridge, plume-ridge interaction, plume pulsing, plume flux, Mid Atlantic Ridge, Iceland Plume, Reykjanes Ridge, North Atlantic, Northern Component Water

A. Analytical Geochemical Techniques

XRF analyses were carried out in the Grant Institute of Earth Science at the University of Edinburgh. The techniques used are similar to those described by Fitton et al. (1998) with modifications noted by Fitton and Godard (2004). Major element concentrations were determined after fusion with a lithium borate flux containing La_2O_3 as a heavy absorber, by a method similar to that developed by Norrish and Hutton (1969). Rock powder was dried at 110°C for at least 1 hour, and a nominal but precisely-weighed 1 g aliquot ignited at 1100°C to determine loss on ignition (LOI). The residue was then mixed with Johnson Matthey Spectroflux™ 105 in a sample:flux ratio of 1:5, based on the unignited sample mass, and fused in a muffle furnace in a Pt5%Au crucible. After the initial fusion, the crucible was reweighed and any flux weight loss was made up with extra flux. After a second fusion over a Meker burner, the molten mixture was swirled several times to ensure homogeneity, cast onto a graphite mold, and flattened with an aluminium plunger into a thin disk. The mold and plunger were maintained at a temperature of 220°C on a hotplate. Trace element concentrations were determined on pressed-powder samples. Eight grams of rock powder were mixed thoroughly with eight drops of a 2% aqueous solution of polyvinyl alcohol. The mixture was loaded into a 40mm diameter aluminium cup in a stainless steel die and compressed against a polished tungsten carbide disc in a hydraulic press at 0.6 t cm^{-2}.

The fused and pressed samples were analyzed using a PANalytical PW 2404 automatic X-ray fluorescence spectrometer with a Rh-anode X-ray tube. Trace-element background positions were placed as close as possible to peaks, and long count times were used at

Jones	Vogt & Hey	Poore	Benediktsdóttir
(VS)R-1	A′	1	Hel
(VS)T-1	A	1′	Sleipnir
(VS)R-2	B	2a+b	Fenrir
(VS)T-2	C	2b′	

Table S1: V-Shaped Ridge naming conventions in Jones et al. (2002) and this paper, Vogt (1971), Hey et al. (2010), Poore et al. (2009) and Benediktsdóttir et al. (2012).

*Corresponding author: tel, +44.121.41.46155
Email address: s.jones.4@bham.ac.uk (S. M. Jones)

both peak and background positions. Where background count rates were measured on either side of the peak, as in most trace-element determinations, the count time was divided between the two positions. Analytical conditions are given in Fitton et al. (1998) and Fitton and Godard (2004). Corrections for matrix effects on the intensities of major-element lines were made using theoretical alpha coefficients calculated on-line using the PANalytical software. The coefficients were calculated to allow for the amount of extra flux replacing volatile components in the sample so that analytical totals should be 100% less the measured LOI. Intensities of the longer wavelength trace element lines (Zn, Cu, Ni, Co, Cr, V, Ba, and Sc) were corrected for matrix effects using alpha coefficients based on major-element concentrations measured at the same time on the powder samples. Matrix corrections were applied to the intensities of the other trace-element lines by using the count rate from the RhK_{α} Compton scatter line as an internal standard (Reynolds, 1963). Line-overlap corrections were applied using synthetic standards.

The spectrometer was calibrated against USGS and CRPG geochemical reference standards using the values given by Govindaraju (1994) except that the values of Jochum et al. (1990) were used for Nb and Zr in BCR-1 and BHVO-1. Excellent calibration lines were obtained using these standards. Analytical precision and accuracy are comparable to the values reported by Fitton et al. (1998) and Fitton and Godard (2004). Four USGS geostandards (BHVO-1, BCR-1, BIR-1, DTS-1) were analysed along with the samples and the data from these (Supplementary Dataset) can be used to assess accuracy and precision.

ICP-MS analyses were carried out at the National Oceanography Centre, Southampton using procedures similar to those described by Murton et al. (2002). Concentrations of minor and rare earth elements were determined on acid-dissolved solutions of whole rocks after cleaning and milling. Calibrations were derived using synthetic standards with a basaltic matrix that matched the samples. Precision (defined as standard deviation divided by mean) was determined from multiple analyses of geological reference materials (BHVO2, BIR-1, JB-1a, JB-3, JGB-1) and ranged from 1.7% (Cs) to 0.2% (Dy) with a mean of 0.6%. Accuracy (measured as the percentage difference between the average and the accepted value of the reference material) ranged between 18.5% (Ta) and 0.9% (Nb) with an average of 5%.

Isotopic analyses were carried out at the National Oceanography Centre, Southampton using multidynamic peak jumping routines on a *VG Sector 54* thermal ionisation mass spectrometers with a constant 2 V beam for ^{88}Sr and a constant 1 V beam for ^{144}Nd. Sample preparation procedures were similar to those described by Murton et al. (2002). Cleaned whole-rock powders were dissolved in hydrofluoric and nitric acid. Powdered sub-samples for strontium analysis were initially leached using dilute hydrochloric acid for 5 hours prior to dissolution to remove any potential strontium contamination from seawater-equilibrated low-temperature alteration phases. For $^{87}Sr/^{86}Sr$ analyses, sample solutions were passed through 50 μl of *Sr-Spec* resin columns to isolate ~1 μg of strontium. The *Sr-Spec* resin column blanks contained less than 0.1 ng strontium. Once dried, the strontium samples were loaded onto a single tantalum filament with a tantalum activator solution. For $^{143}Nd/^{144}Nd$ analyses, sample solutions were passed through a two-column procedure; the first using a cation exchange resin was followed by a *Ln Spec* column to isolate ~1 μg of neodymium. The procedural blanks for both columns contained <0.3 ng neodymium in total. The samples were then loaded on to the tantalum sides of a tantalum-rhenium-tantalum triple-laminated filament assembly. External reproducibility during the period of these analyses was maintained at 0.710265 ± 25 (2 s.d., n = 142) for the international reference standard NBS-987 (for $^{87}Sr/^{86}Sr$), and 0.512092 ± 15 (2 s.d., n = 78) for the international reference standard, JNdi (for $^{143}Nd/^{144}Nd$). Both strontium and neodymium isotopes were normalized to $^{87}Sr/^{86}Sr$ = 0.1194 and $^{143}Nd/^{144}Nd$ = 0.7219 respectively.

B. Composition and Melting: Additional Figures

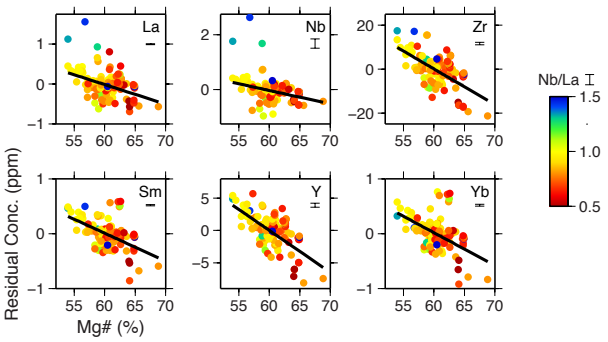

Figure S1: Effect of fractional crystallization. Residual concentration is difference between measured concentration and associated non-parametric regression line. Error bars are 2σ ranges from repeat measurements of samples BRR1 (XRF) and BIR-1 (ICPMS). Regression lines are for the subset 0.8 < Nb/La < 1.2.

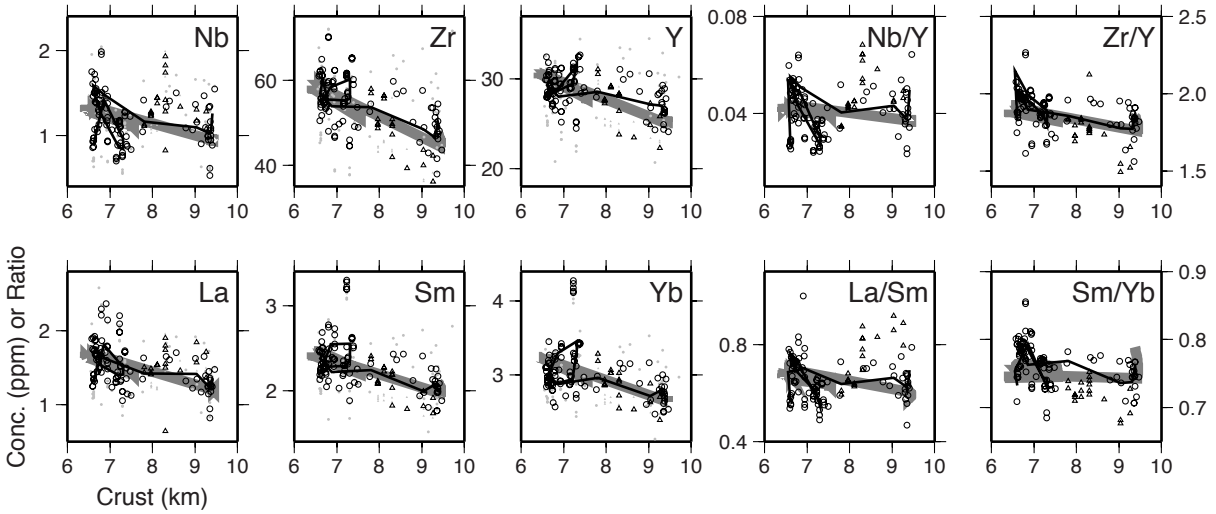

Figure S2: Relationship between composition and crustal thickness. Small grey dots: raw data. Circles: data along spreading axis corrected for fractional crystallization. Black line: spreading axis data (circles) smoothed using a box-car filter, width 50 km. Grey line: model prediction. Triangles: data along VSR2 crest corrected for fractional crystallization.

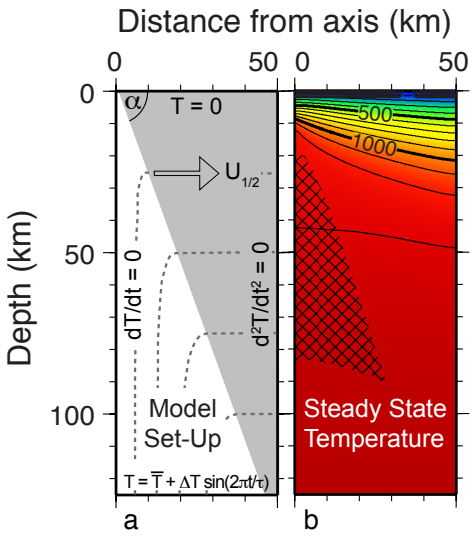

Figure S3: (a) 2D model geometry, mantle flow field (dashed lines) and temperature boundary conditions. (b) Steady-state temperature field for T_P = 1313°C. Melting region is shown cross-hatched.

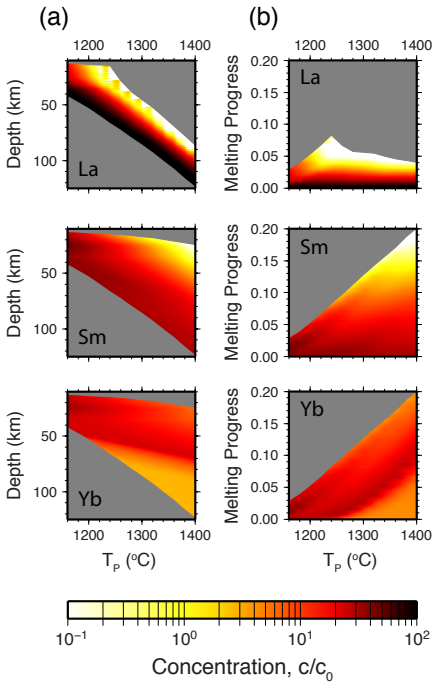

Figure S4: Instantaneous melt composition, $c\,(X(z)\,,T_{P0})$, grids used to calculate average erupted melt compositions (Section 6). Compositions calculated as ratios of c to source concentration c_0. (a) Composition grids for La, Sm and Yb as functions of and depth z and mantle potential temperature at base of model T_{P0}. (b) Corresponding composition grids on axes of melting progress X and T_{P0}.

C. Method of Comparing Modelled and Observed Compositions

Model compositions are calculated as ratios of concentrations to source concentrations. They need to be compared with observations, which recorded as concentrations. The problem is that we do not know the source

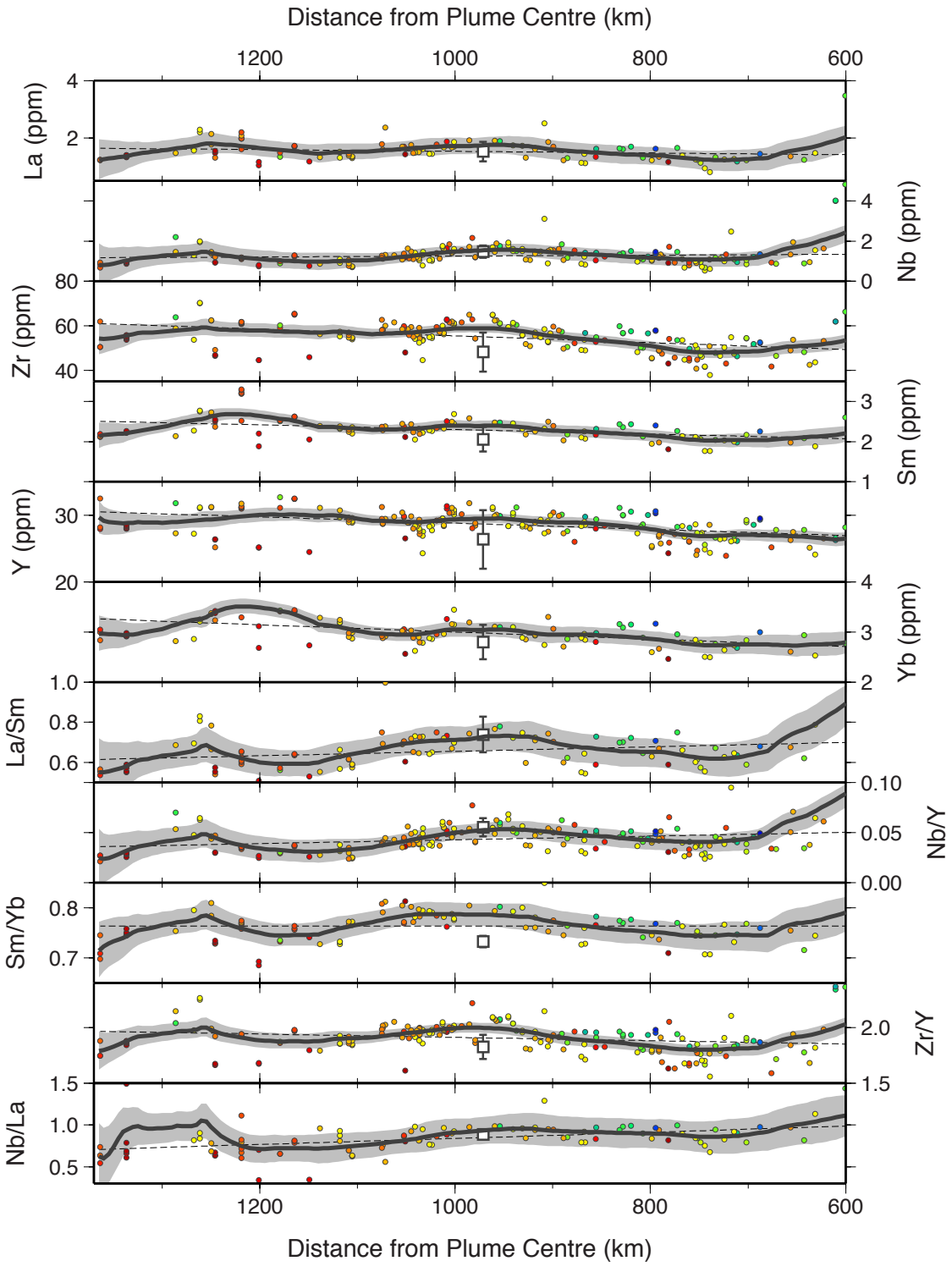

Figure S5: Compositional dataset used to determine the results plotted in Figure 10. Small circles are data points from dredge samples along the spreading axis, coloured according to Mg#. Large square with vertical error bar is the composition at the crest of VSR-2 off-axis along a plate spreading flow line from the MAR/VST-1 intersection. Element concentrations were corrected to Mg# = 60% using the regression lines in Figure 5. Thin dashed lines show the linear trends in the data. Thick lines and grey confidence envelopes from the non-parametric regression technique of Samworth and Poore (2005).

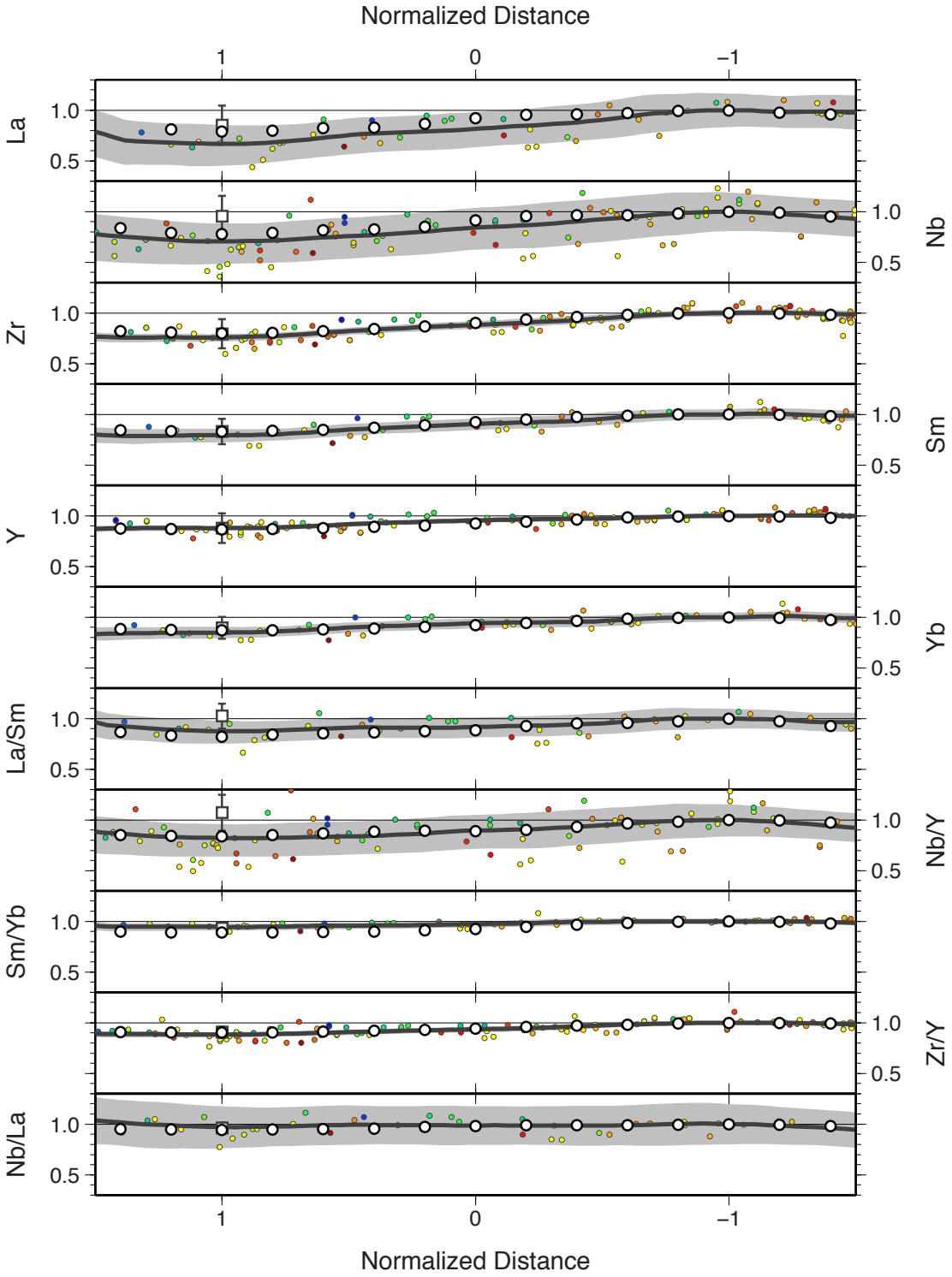

Figure S6: Transformation of the data in Figure S3, from which values plotted in Figure 10 were extracted. This example has the MAR/VSR-1intersection at distance 1 and the MAR/VST-1intersection at distance −1, and corresponds to the large square symbols on Figure 10. Small coloured circles show observations, large while circles show modelled compositions.

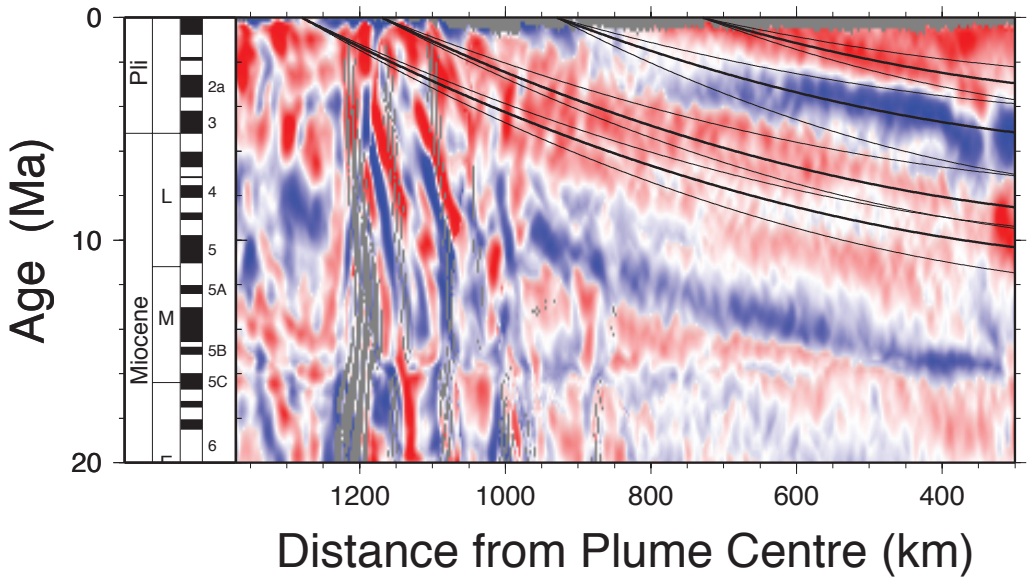

Figure S7: VSR models fitted to gravity proxy for crustal structure. A set of 3 lines for each V-shaped ridge and trough shows the best fitting model and bounds.

composition *a priori*. This problem can be avoided by comparing amplitudes of periodic compositional variation expressed as ratios, i.e. minimum:maximum concentrations.

Figure S5 shows the compositional data used to calculate the observed amplitudes of periodic variation. Three transformations were applied to generate Figure S6. First, a straight line regression was fitted to each dataset and the dataset then rotated so as to flatten this linear trend. This procedure was carried out to isolate the periodic component of the compositional variation from any regional trends. Secondly, distances were normalized so that the V-Shaped Ridge/MAR intersection lay at 1 and the V-Shaped Trough/MAR intersection lay at −1. This transformation aligns the minima and maxima, which are not expected to be exactly aligned to begin with. Thirdly, compositions were normalized by the concentration (ratio) of the non-parametric regression line at a normalized distance of −1.

There was no need to remove a background linear trend from the modelled compositions. One cycle (5 My) of model compositional data was extracted and model time normalized to give maximum and mimumum concentrations at −1 and 1. Compositions were normalized in the same way as the observed compositions.

Values plotted on Figure 9 were read off Figure S6 at a distance of 1. The error bars on the axial observations were taken from the confidence bands at the same distance. The error bars on the off-axis observations are normalized standard deviations of the sample group.

VSR	Intersection (km)	Start Time (Ma)	Volume Flux ($km^3\ yr^{-1}$)	T_{P0} (°C)	ΔT (°C)
VSR-1	730	3.8 ± 1.0	50 ± 13	1327	27
VST-1	930	6.4 ± 1.9	49 ± 14	1315	21
VSR-2	1170	9.1 ± 1.3	49 ± 7	1309	14
VST-2	1280	11.3 ± 1.1	47 ± 5	1306	11

Table S2: VSR modelling parameters. MAR intersection, start time and volume flux define planform geometry models in Figure 4. Potential temperature T_{P0} and temperature fluctuation ΔT define time-dependent melting models in Figure 8.

D. Volume Flux Estimates

Estimates of plume volume flux were obtained using a kinematic model in which the plume head spreads radially outward within an asthenosphere channel (White and Lovell, 1997; Rudge et al., 2008). Here, we modified the basic model to account for the fact the the plume centre does not lie on the spreading axis. The modified model has Cartesian coordinates, with the spreading axis along the y axis and the plume centre at (x_p, y_p). We set $x_p = 200$ km, from the plume centre position estimated by Shorttle et al. (2010), and define $y_p = 0$. The position of a thermal pulse as it travels along the spreading axis is $y(t)$, given by

$$y = \sqrt{kt - x_p^2} + y_p \tag{S1}$$

Time t is the time after the thermal pulse left the plume centre, which is related to geological age, measured backward from present, by $a = a_0 - t$. The geological age when the temperature pulse began travelling outward from the plume centre is given by

$$a_0 = \frac{\left(y_0 - y_p\right)^2 + x_p^2}{k} \tag{S2}$$

where y_0 is the distance of the present-day intersection of the VSR with the spreading axis. Values of y_0 were taken from Figure 4. The model has one parameter k that is adjusted to fit the VSR gravity data (Figure S7). k can be transformed to plume volume flux using

$$Q = \pi k h \tag{S3}$$

where $h = 100$ km is the thickness of the plume head channel. Rudge et al. (2008) discuss the reasons for choosing $h = 100$ km.

References

Benediktsdóttir, A., Hey, R., Martinez, F., Höskuldsson, A., 2012. Detailed tectonic evolution of the Reykjanes Ridge during the past 15 Ma. Geochemistry, Geophysics, Geosystems 13 (2), Q02008.

Fitton, J., Godard, M., 2004. Origin and evolution of magmas on the Ontong Java Plateau. In: Fitton, J. G., Mahoney, J., Wallace, P., Saunders, A. (Eds.), Origin and Evolution of the Ontong Java Plateau. Vol. 229 of Geological Society, London, Special Publications. pp. 151–178.

Fitton, J., Saunders, A., Larsen, L., Hardarson, B., Norry, M., 1998. Volcanic rocks from the southeast Greenland margin at 63∘N: composition, petrogenesis and mantle sources. Proceedings of the Ocean Drilling Program, Scientific Results 152, 331–350.

Govindaraju, K., 1994. 1994 compilation of working values and sample description for 383 geostandards. Geostandards Newsletter 18, 1–158.

Hey, R., Martinez, F., Höskuldsson, A., Benediktsdóttir, A., 2010. Propagating rift model for the V-shaped ridges south of Iceland. Geochemistry, Geophysics, Geosystems 11 (3), Q03011.

Jochum, K., Seufert, H., Thirlwall, M., 1990. High-sensitivity Nb analysis by spark-source mass spectrometry (SSMS) and calibration of XRF Nb and Zr. Chemical Geology 81, 1–16.

Jones, S. M., White, N., Maclennan, J., 2002. V-shaped ridges around iceland: Implications for spatial and temporal patterns of mantle convection. Geochemistry, Geophysics, Geosystems 3 (10), 1059.

Murton, B., Taylor, R., Thirlwall, M., 2002. Plume-ridge interaction: A geochemical perspective from the Reykjanes Ridge. Journal of Petrology 43 (11), 1987–2012.

Norrish, K., Hutton, J., 1969. An accurate X-ray spectrographic method for the analysis of a wide range of geological samples. Geochimica et Cosmochimica Acta 33, 431–453.

Poore, H., White, N., Jones, S., 2009. A Neogene chronology of Iceland plume activity from V-shaped ridges. Earth and Planetary Science Letters 283, 1–13.

Reynolds, R., 1963. Matrix corrections in trace element analysis by x-ray fluorescence: estimation of the mass absorption coefficient by Compton scattering. American Mineralogist 48, 1133–1143.

Rudge, J. F., Shaw Champion, M., White, N., McKenzie, D., Lovell, B., 2008. A plume model of transient diachronous uplift at the Earth's surface. Earth and Planetary Science Letters 267, 146—160.

Samworth, R., Poore, H., 2005. Understanding past ocean circulations: a nonparametric regression case study. Statistical Modelling 5, 289–307.

Shorttle, O., Maclennan, J., Jones, S. M., 2010. Control of the symmetry of plume-ridge interaction by spreading ridge geometry. Geochemistry, Geophysics, Geosystems 11, Q0AC05.

Vogt, P. R., 1971. Asthenosphere motion recorded by the ocean floor south of Iceland. Earth and Planetary Science Letters 13, 153–160.

White, N., Lovell, B., 1997. Measuring the pulse of a plume with the sedimentary record. Nature 387, 888–891.